Twistronics of Janus transition metal dichalcogenide bilayers

Mattia Angeli [●],[1] Gabriel R. Schleder [●],[1] and Efthimios Kaxiras[1,2]

[1]*John A. Paulson School of Engineering and Applied Sciences, Harvard University, Cambridge, Massachusetts 02138, USA*
[2]*Department of Physics, Harvard University, Cambridge, Massachusetts 02138, USA*

Twisted multilayers of two-dimensional (2D) materials are an increasingly important platform for investigating quantum phases of matter, and in particular, strongly correlated electrons. The moiré pattern introduced by the relative twist between layers creates effective potentials of long wavelength, leading to electron localization. However, in contrast to the abundance of 2D materials, few twisted heterostructures have been studied until now. Here we develop a first-principles continuum theory to study the electronic bands introduced by moire patterns of twisted Janus transition metal dichalcogenide (TMD) homo- and heterobilayers. The model includes lattice relaxation, stacking-dependent effective mass, and Rashba spin-orbit coupling. We then perform a high-throughput generation and characterization of DFT-extracted continuum models for more than a hundred possible combinations of materials and stackings. Our model predicts that the moiré physics and emergent symmetries depend on chemical composition, vertical layer orientation, and twist angle, so that the miniband wave functions can form triangular, honeycomb, and kagome networks. Rashba spin-orbit effects, peculiar of these systems, can dominate the moiré bandwidth at small angles. Our work enables detailed investigation of Janus twisted heterostructures, allowing the discovery and control of novel electronic phenomena.

I. INTRODUCTION

Strong interactions between particles are a central pillar of quantum physical phenomena, leading to many different phases of matter, such as superconductors and fractional quantum Hall states [1,2]. These phenomena are investigated in condensed-matter systems in the so-called quantum materials [3–5], where quantum effects dominate their properties. These properties can in turn be tuned through materials-engineering "knobs" that pertain to each type of material, such as chemical composition, structural changes, and external perturbations.

Recently, two-dimensional few-layer systems, such as graphene and transition metal dichalcogenides (TMDs), have proven to be one of the leading platforms to study many of these effects, owing to their low dimensionality. The possibility to manipulate interlayer interactions of van der Waals (vdW) materials by changing the twist angle between two layers has been triggered by the breakthroughs in magic-angle graphene multilayers [6–16]. In these systems, the relative twist angle results in a moiré superlattice, which acts as a long-wavelength modulating potential changing the electronic, vibrational, and structural properties [17–19]. Flat bands, nontrivial topology, emergent symmetries, enhanced correlations, and strong electron-phonon coupling can arise as a result of the charge localization induced by the moiré superlattice [20–28].

Indeed, recent experiments have moved beyond graphene. As an example, work on twisted TMDs quickly uncovered a plethora of novel phenomena, such as correlated insulating states, quantum anomalous Hall states, superconductivity, and moiré excitons [29–34]. Given the huge number of possible combinations to create these moiré materials [35,36] and the experimental challenges in achieving them, only a small subset of systems has been studied to date. Nonetheless, by creating moiré structures with different properties in their individual constituents, new physical properties are possible in the interacting system.

Transition-metal dichalcogenide layers with different chalcogen atoms on either side of the metal plane [37], referred to as "Janus" layers [38], have attracted intense interest due to their special properties introduced by the broken mirror symmetry of the corresponding pure layers [37]. Compared to MX_2 monolayers with D_{3v} symmetry such as MoS_2, Janus group-VI chalcogenides MXY (X, Y = S, Se, Te; X $\neq$ Y) are noncentrosymmetric compounds with C_{3v} symmetry [13]. The difference in electronegativity between the two chalcogen layers leads to a built-in electric dipole oriented in the out-of-plane direction, generating strong Rashba spin-orbit couplings (SOC). Furthermore, the intrinsic electric field provides an additional degree of freedom with which to tune the van der Waals interaction between adjacent layers. As such, these systems present ingredients and properties to the already-known tuning knobs available for probing moiré-driven phenomena.

In this paper we present results from an *ab initio* continuum model designed for twisted Janus TMDs. The model extends the one-band continuum Hamiltonian of Refs. [39,40] to better capture the rich physics of polar TMDs. A set of inexpensive bilayer calculations is used to compute the electronic and structural potentials which are then used to include lattice relaxation and compute the band structure. The effective mass approximation of the band edges is relaxed by the inclusion of a moiré-dependent term. The flat bands of these systems are

TABLE I. Bulk ($\mathcal{K}$) and shear moduli ($\mathcal{G}$), in meV per unit cell, of the six Janus TMD monolayers considered.

|	MoSSe	WSSe	MoSTe	WSTe	MoSeTe	WSeTe
$\mathcal{K}$	49.7	45.8	39.7	42.7	41.7	39.1
$\mathcal{G}$	34.2	30.7	25.4	29.6	27.7	27.7

thoroughly analyzed and characterized in terms of the symmetries and centers of the corresponding Wannier orbitals. Finally, we create a database of relevant physical parameters that can be used as a reference to reproduce the continuum model bands of more than a hundred twisted bilayers, and also to guide experimental and theoretical efforts toward those systems which exhibit the most interesting physics. Additionally, the models presented in this work can serve as a starting point to study the quantum phases of twisted Janus materials with Hartree-Fock [28,41–47] and exact diagonalization [48,49] techniques, or to derive a small set of Wannier orbitals [50] used in density-matrix renormalization group calculations that treat strong correlations [51–56].

The work is organized as follows: In Sec. II we start by briefly introducing the geometrical features of twisted bilayers. In Sec. II A we focus on the continuum model Hamiltonian and the methodology employed to obtain its potentials from *ab initio* calculations. In Sec. II B we discuss a set of twisted bilayers in which Rashba SOC is negligible and the moiré bands develop emergent symmetries. In Sec. II C we focus on those bilayers in which Rashba effects are important. The last section (Sec. III) is devoted to discussing some of the exotic physics that could be observed in these systems. The parameters that characterize the continuum models of more than a hundred of the twisted bilayers are listed in Tables II and III.

II. RESULTS

Twisted heterostructures between TMD monolayers occur in two distinct configurations [57], known as 2H and 3R. The two configurations differ by a 180° rotation of the top layer around a vertical axis passing through the position of the transition metal atom and are not related by any shift of one layer with respect to the other. In Fig. 1 we show 3R and 2H twisted bilayers. In the 3R configuration, the perfectly aligned areas called AA are surrounded by six Bernal-stacked regions (MX and XM) that form a honeycomb network. In the MX/XM areas, a metal atom (M) on one layer is directly on top/below a chalcogen atom (X) on the other layer. The two regions are related by a reflection that exchanges the two layers. In 2H bilayers, metal/chalcogen atoms are on top of each other in the MM/XX Bernal stacked regions. Vertical alignment between the layers is obtained in the AB regions, where different atoms are on top of each other. In both configurations, the interface regions between Bernal domains are the so-called domain walls (DWs) which form a kagome network.

In general, the geometry of the moiré pattern is characterized by the presence of high-symmetry regions orderly distributed to form hexagonal Bravais lattices [58]. The AA/AB regions form a triangular network, while two adjacent
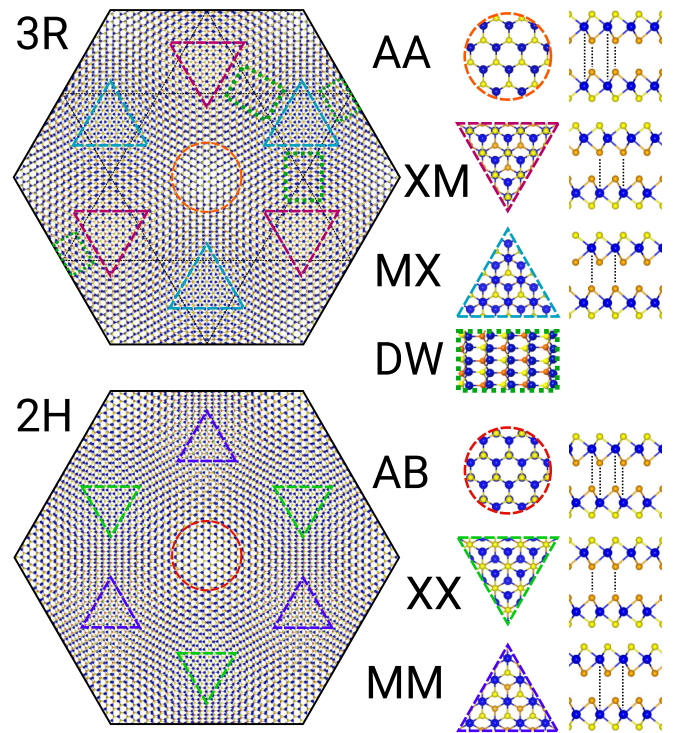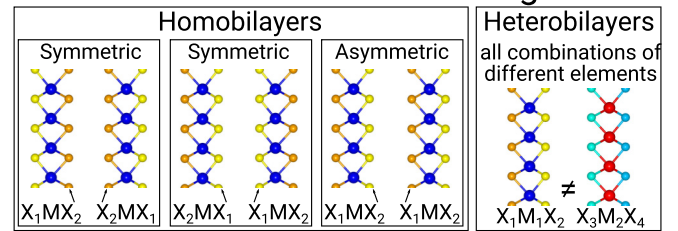

FIG. 1. Moiré superlattices created by twisting TMD bilayers and possible interface orderings of Janus TMDs. Two different configurations are possible, 3R or 2H. From an aligned reference, these two configurations differ by a 180° rotation of one layer. The high-symmetry stacking regions of each superlattice are highlighted with dashed circles and triangles, together with the corresponding top and side views. In 3R twisted bilayers, perfect layer alignment is found in the AA regions. MX/XM are Bernal-stacked areas in which a metal atom is on top/below a pair of chalcogens. These regions form a hexagonal pattern. At the interface between Bernal domains lie the domain wall (DW) regions. Three of these areas are highlighted in dotted green. As pointed out by black lines, the DWs form a kagome network. In 2H twisted bilayers, the horizontal displacement of two layers overlaps in the AB regions, where metal and chalcogens lie on top of each other. In the XX/MM Bernal domains, only the chalcogen/metal layers align.

MX/XM or XX/MM regions are the basis of a honeycomb lattice. Finally, the DW centers correspond to the three-site basis of a kagome lattice.

Unlike in nonpolar TMDs, the electronic properties of Janus bilayers depend on how the chalcogen layers are vertically ordered [59]. This ordering will determine the interface and interlayer interactions between the layers, dictating where the valence band maximum and conduction band minimum (VBM/CBM) are located in momentum space.

TABLE II. Homobilayer continuum model parameters. The first line for each material corresponds to the valence band edge (VBM), which occurs at Γ, and the second line corresponds to the conduction band edge (CBM), which occurs at K. The exceptions to this rule are marked by an asterisk, in which case both the VBM and CBM occur at K. The GSFE (Ω) and moiré potential (Δ) Fourier coefficients (modulus and phase ϕ) are listed up to the third moiré G-vectors shell. The effective mass (m_0^*) and potential (ε) Fourier coefficient are in bare electron mass units. The Rashba coefficient (α_R) is in meV/Å. The moiré superlattice (MSL) formed by the topmost/lowest valence/conduction band's localized charge distribution is listed in the last column, where T stands for triangular, H for honeycomb, and K for kagome.

Material	Stack ordering	Band Edge	$W_{1,2,3}$	$\phi_W^{1,2,3}$	$V_{1,2,3}$	$\phi_V^{1,2,3}$	m_0^*	U_1	ϕ_U^1	α_R	MSL
3R MoSSe	Se-S-Se-S	Γ @ VB	(8.7,0.2,0.1)	(1.0,0.2, 2.6)	(3.6,0.1,0.1)	(74.6,62.5,10.6)	-0.1	0.01	163.5	66.3	T @ MX
		K @ CB	(8.7,0.2,0.1)	(1.0,0.2, 2.6)	(3.7,0.14,0.16)	(92.3,81.0,87.3)	0.92	0.01	2.6	0.0	T @ MX
	S-Se-Se-S	Γ @ VB	(7.4,1.0,0.1)	(0.0,180.0,180.0)	(8.7,0.1,1.7)	(180.,-180.0,0.0)	-0.37	0.01	0.0	0.0	H @ MX/XM
		K @ CB	(7.4,1.0,0.1)	(0.0,180.0,180.0)	(5.9,0.6,0.2)	(0.0,180.0,0.0)	0.37	0.08	0.0	0.0	H @ MX/XM
	Se-S-S-Se	Γ @ VB	(6.1,0.2,0.2)	(0.0,0.0, 0.0)	(7.8,0.2,0.3)	(0.0,0.0,0.0)	-0.4	0.01	0.0	0.0	T @ AA
		K @ CB	(6.1,0.2,0.2)	(0.0,0.0, 0.0)	(0.5,1.1,0.51)	(0.0,180.0,0.0)	0.65	0.01	180.0	0.0	H @ MX/XM
2H MoSSe	Se-S-Se-S	Γ @ VB	(7.9,0.1,0.1)	(131.9, 1.2, 85.4)	(4.9,0.1,0.1)	(125.9,156.9,140.5)	-0.36	0.0	0.0	16.6	T @ MM
		K @ CB	(7.9,0.1,0.1)	(131.9, 1.2, 85.4)	(0.7,0.3,0.1)	(122.2,175.5,73.0)	0.83	0.01	144.0	0.0	T @ XX
	S-Se-Se-S	Γ @ VB	(7.5,1.3,0.4)	(143.7, 180.0, 87.5)	(11.9,0.96,1.3)	(58.5,175.5,116.0)	-0.42	0.02	180.0	0.0	T @ AB
		K @ CB	(7.5,1.3,0.4)	(143.7, 180.0, 87.5)	(5.9,0.6,0.2)	(115.0,8.6,38.8)	0.29	0.06	150.0	0.0	T @ XX
	Se-S-S-Se	Γ @ VB	(8.9,1.4,0.2)	(129.2, 180.0, 46.7)	(35.0,14.5,7.7)	(60.5,0.8,128.0)	-0.62	0.08	127.6	0.0	T @ XX
		K @ CB	(8.9,1.4,0.2)	(129.2, 180.0, 46.7)	(0.7,0.0,0.2)	(24.0,7.3,64.8)	0.5	0.03	122.9	0.0	T @ MM
3R WSSe	Se-S-Se-S*	K @ VB	(8.3,0.2,0.1)	(0.0,0.0, -2.4)	(4.9,0.6,0.9)	(92.9,-162.7,-56.7)	-2.64	0.0	0.0	0.0	T @ XM
		K @ CB	(8.3,0.2,0.1)	(0.0,0.0, -2.4)	(3.8,0.2,0.2)	(-79.1,39.7,93.9)	2.07	0.01	-2.5	0.0	T @ XM
	S-Se-Se-S	Γ @ VB	(7.6,1.3,0.6)	(0.0,-180.0, -180.0)	(8.9,2.8,0.5)	(180.0,180.0,0.0)	-0.7	0.02	0.0	0.0	K @ DW
		K @ CB	(7.6,1.3,0.6)	(0.0,-180.0, -180.0)	(2.6,0.8,1.5)	(0.0,0.0,0.0)	1.19	0.02	0.0	0.0	H @ XM/XM
	Se-S-S-Se	Γ @ VB	(6.0,0.1,0.1)	(0.0,0.0,0.0)	(7.9,0.2,0.06)	(0.0,0.0,-120.0)	-0.82	0.01	0.0	0.0	T @ AA
		K @ CB	(6.0,0.1,0.1)	(0.0,0.0,0.0)	(2.4,2.6,1.3)	(0.0,180.0,0.0)	1.9	0.01	180.0	0.0	H @ XM/XM
2H WSSe	S-Se-S-Se*	K @ VB	(8.3,0.2,0.1)	(0.0, 0.0, -2.0)	(0.7,0.4,0.3)	(-168.0,-71.0,142.5)	-2.63	0.0	0.0	0.0	T @ XX
		K @ CB	(8.3,0.2,0.1)	(0.0, 0.0, -2.0)	(1.2,0.1,0.2)	(-160.5,-66.1,-134.9)	2.1	0.01	115.0	0.0	T @ AB
	S-Se-Se-S	Γ @ VB	(7.2,0.1,0.7)	(148.1, -109.9, 60.5)	(3.6,1.2,1.5)	(93.4,178.9,29.7)	-0.72	0.03	125.0	0.0	T @ M
		K @ CB	(7.2,0.1,0.7)	(148.1, -109.9, 60.5)	(2.8,0.8,0.2)	(113.4,5.0,-45.1)	1.3	0.05	132.3	0.0	T @ MM
	Se-S-S-Se	Γ @ VB	(7.8,1.9,0.5)	(127.7, 180.0, 75.5)	(20.2,20.6,9.5)	(-66.6,0.0,-125.7)	-0.99	0.07	125.0	0.0	T @ XX
		K @ CB	(7.8,1.9,0.5)	(127.7, 180.0, 75.5)	(0.8,0.1,0.1)	(-23.7,164.1,60.0)	2.0	0.06	55.0	0.0	T @ MM
3R MoSTe	Te-S-Te-S	Γ @ VB	(10.9,1.8,0.5)	(-7.4,180.0, 177.4)	(4.9,0.7,0.5)	(-29.0,26.4,-171.9)	-0.2	0.0	0.0	0.0	T @ AA
		K @ CB	(10.9,1.8,0.5)	(-7.4,180.0, 177.4)	(3.7,0.1,0.1)	(92.1,-86.9,81.9)	0.96	0.01	-2.5	0.0	T @ MX
	Te-S-S-Te	Γ @ VB	(6.4,0.2,0.2)	(0.0,0.0, 0.0)	(12.6,0.1,0.4)	(0.0,-67.1,2.2)	-1.0	0.02	0.0	0.0	T @ AA
		K @ CB	(6.4,0.2,0.2)	(0.0,0.0, 0.0)	(0.5,1.1,0.5)	(0.0,180.0,0.0)	0.68	0.01	180.0	0.0	H @ MX/XM
	S-Te-Te-S	Γ @ VB	(9.0,1.6,0.3)	(0.0,180.0, 180.0)	(1.5,0.4,0.2)	(180.0,0.0,-165.2)	-0.19	0.01	180.0	0.0	H @ MX/XM
		K @ CB	(9.0,1.6,0.3)	(0.0,180.0, 180.0)	(4.3,1.6,0.2)	(0.0,180.0,0.0)	0.1	0.08	0.0	0.0	H @ MX/XM
2H MoSTe	S-Te-S-Te*	K @ VB	(9.9,2.4,1.4)	(136.2, 180.0, 53.6)	(5.2,0.4,0.2)	(-128.5,153.4,-137.9)	-2.3	0.0	0.0	0.0	T @ MM
		K @ CB	(9.9,2.4,1.4)	(136.2, 180.0, 53.6)	(4.8,4.3,2.0)	(114.5,0.0,-128.4)	1.2	0.1	-107.7	0.0	T @ AA
	Te-S-S-Te	Γ @ VB	(10.9,2.0,0.7)	(112.2, 180.0, 20.8)	(43.5,13.5,12.4)	(90.5,0.0,-138.9)	-1.49	0.17	-104.4.0	0.0	T @ AB
		K @ CB	(10.9,2.0,0.7)	(112.2, 180.0, 20.8)	(1.36,0.98,0.68)	(49.8,180.0,27.5)	1.07	0.01	40.7	0.0	T @ XX
	S-Te-Te-S	Γ @ VB	(9.4,1.4,0.56)	(155.3, 180.0, 129.0)	(1.21,0.22,0.28)	(7.6,3.0,14.6)	-0.3	0.01	155.0	0.0	T @ MM
		K @ CB	(9.4,1.4,0.56)	(155.3, 180.0, 129.0)	(3.64,0.33,0.36)	(122.8,172.0,55.5)	0.13	0.09	178.9	0.0	T @ MM
3R WSTe	Te-S-Te-S*	K @ VB	(9.5,1.86,0.8)	(142.4,180.0, 114.7)	(1.1,0.65,1.1)	(152.4,-21.3,-64.8)	-2.02	0.01	40.0	0.0	T @ XM
		K @ CB	(9.5,1.86,0.8)	(142.4,180.0, 114.7)	(1.64,0.53,0.75)	(-143.1,9.0,75.5)	0.96	0.01	-2.5	0.0	T @ AA
	Te-S-S-Te	Γ @ VB	(9.6,2.8,2.0)	(0.0,180.0, 0.0)	(14.7,33.6,13.4)	(180.0,0.0,180.0)	-1.3	0.09	0.0	0.0	H @ MX/XM
		K @ CB	(9.6,2.8,2.0)	(0.0,180.0, 0.0)	(1.1,2.2,1.4)	(0.0,180.0,0.0)	1.52	0.0	0.0	0.0	H @ MX/XM
	S-Te-Te-S	Γ @ VB	(8.6,1.1,0.16)	(0.0,180.0, 0.0)	(2.5,0.5,0.3)	(130.0,0.0,-135.2)	-0.3	0.01	180.0	0.0	T @ MX
		K @ CB	(8.6,1.1,0.16)	(0.0,180.0, 0.0)	(6.7,2.6,0.8)	(0.0,180.0,180.0)	0.42	0.07	0.0	0.0	H @ MX/XM
2H WSTe	S-Te-S-Te*	K @ VB	(9.5,1.9,0.8)	(142.5, 180.0, 114.7)	(1.1,0.6,1.1)	(152.5,-21.0,-64.4)	-2.0	0.01	40.2	0.0	T @ MM
		K @ CB	(9.5,1.9,0.8)	(142.5, 180.0, 114.7)	(1.6,0.5,0.75)	(-141.1,9.0,75.4)	1.6	0.02	112.7	0.0	T @ AA
	Te-S-S-Te	Γ @ VB	(9.3,1.3,0.2)	(116.2, 180.0, 0.0)	(37.7,8.9,2.9)	(-82.5,0.0,-171.1)	-1.52	0.13	110.4	0.0	T @ XX
		K @ CB	(9.3,1.3,0.2)	(116.2, 180.0, 0.0)	(2.85, 0.4,0.2)	(-62.8,0.0,-107.5)	1.54	0.02	45.7	0.0	T @ MM
	S-Te-Te-S	Γ @ VB	(9.4,1.4,0.6)	(155.3, 180.0, 129.0)	(0.2,0.4,0.2)	(140.6,24.0,14.6)	-0.4	0.02	70.0	0.0	T @ XX
		K @ CB	(9.4,1.4,0.6)	(155.3, 180.0, 129.0)	(6.7,0.3,0.3)	(148.8,-169.0,20.5)	0.36	0.12	176.9	0.0	T @ AB

TABLE II. (*Continued.*)

Material	Stack ordering	Band Edge	$W_{1,2,3}$	$\phi_W^{1,2,3}$	$V_{1,2,3}$	$\phi_V^{1,2,3}$	m_0^*	U_1	ϕ_U^1	α_R	MSL
3R WSeTe	Te-Se-Te-Se	Γ @ VB	(11.8,1.7,1.25)	(2.4,180.0,8.6)	(30.7,1.9,5.5)	(-177.0,-168.4,35.7)	-0.4	0.0	0.0	0.0	T @ MX
		K @ CB	(11.8,1.7,1.25)	(2.4,180.0,8.6)	(1.6,0.5,0.8)	(-143.1,9.0,75.5)	0.96	0.01	-2.5	0.0	T @ MX
	Te-Se-Se-Te	Γ @ VB	(9.6,2.8,2.0)	(0.0,180.0,0.0)	(14.7,33.6,13.4)	(180.0,0.0,180.0)	-1.3	0.09	0.0	0.0	H @ MX/XM
		K @ CB	(9.6,2.8,2.0)	(0.0,180.0,0.0)	(1.1,2.2,1.36)	(0.0,180.0,0.0)	1.52	0.0	0.0	0.0	H @ MX/XM
	Se-Te-Te-Se	Γ @ VB	(11.2,0.3,0.4)	(0.0,180.0,0.0)	(3.9,5.2,5.7)	(180.0,0.0,0.0)	-0.9	0.07	0.0	0.0	T @ AA
		K @ CB	(11.2,0.3,0.4)	(0.0,180.0,0.0)	(1.4,1.8,1.6)	(0.0,180.0,0.0)	1.6	0.01	180.0	0.0	H @ MX/XM
2H WSeTe	Se-Te-Se-Te	Γ @ VB	(10.3,0.8,1.0)	(151.2,-172.0,-103.7)	(24.5,4.7,6.0)	(-55.5,-6.0,-155.4)	-0.3	0.13	123.4	107.4	T @ XX
		K @ CB	(10.3,0.8,1.0)	(151.2,-172.0,-103.7)	(3.6,0.5,0.6)	(-78.9,-165.9,20.4)	1.7	0.03	94.7	0.0	T @ XX
	Te-Se-Se-Te	Γ @ VB	(12.0,0.7,0.5)	(160.0,-167.0,-48.0)	(9.9,2.7,1.6)	(-9.0,34.5,90.0)	-0.3	0.03	70.0	0.0	T @ AB
		K @ CB	(12.0,0.7,0.5)	(160.0,-167.0,-48.0)	(5.2,0.4,0.3)	(-153.9,174.0,-58.5)	0.9	0.12	166.7	0.0	T @ AB
	Se-Te-Te-Se	Γ @ VB	(9.1,0.7,0.2)	(128.3,180.0,-43.0)	(21.1,3.4,1.4)	(-65.3,-177.0,-142.1)	-0.9	0.07	125.0	0.0	T @ XX
		K @ CB	(9.1,0.7,0.2)	(128.3,180.0,-43.0)	(22.5,23.3,11.0)	(-62.5,78.0,-107.5)	1.7	0.01	76.9	0.0	T @ MM
3R MoSeTe	Te-Se-Te-Se	Γ @ VB	(11.4,2.1,1.3)	(-3.8,180.0,9.6)	(55.7,6.1,5.4)	(177.7,-173.9,36.9)	-0.17	0.15	0.0	70.3	T @ MX
		K @ CB	(11.4,2.1,1.3)	(-3.8,180.0,9.6)	(22.4,8.5,3.8)	(19.1,2.0,1.1)	0.4	0.07	3.5	0.0	T @ MX
	Te-Se-Se-Te	Γ @ VB	(11.8,0.1,1.0)	(0.0,0.0,0.0)	(6.3,9.3,14.4)	(180.0,180.0,180.0)	-0.8	0.06	0.0	0.0	T@MX
		K @ CB	(11.8,0.1,1.0)	(0.0,0.0,0.0)	(0.8,0.6,0.7)	(0.0,180.0,0.0)	3.9	0.0	0.0	0.0	H @ MX/XM
	Se-Te-Te-Se	Γ @ VB	(8.9,1.1,0.2)	(0.0,180.0,0.0)	(5.6,1.5,0.5)	(180.0,0.0,180.0)	-0.1	0.03	0.0	0.0	H @ MX/XM
		K @ CB	(8.9,1.1,0.2)	(0.0,180.0,0.0)	(1.75,0.6,0.8)	(0.0,0.0,0.0)	4.6	0.02	180.0	0.0	T @AA
2H MoSeTe	Se-Te-Se-Te	Γ @ VB	(11.5,0.7,0.6)	(146.2,-167.0,-61.9)	(32.5,4.0,3.9)	(-45.5,-178.0,105.4)	-0.02	0.09	143.4.0	104.2	T @ AB
		K @ CB	(11.5,0.7,0.6)	(146.2,-167.0,-61.9)	(18.1,9.2,4.4)	(130.1,1.7,-101.4)	4.5	0.03	145.7	0.0	T @ XX
	Te-Se-Se-Te	Γ @ VB	(11.9,0.0,0.9)	(0.0,0.0,0.0)	(6.5,9.5,14.5)	(180.0,180.0,180.0)	-0.8	0.06	0.0	0.0	T @ MM
		K @ CB	(11.9,0.0,0.9)	(0.0,0.0,0.0)	(0.6,0.4,0.1)	(-161.9,2.0,-138.5)	4.9	0.01	-107.7	0.0	T @ MM
	Se-Te-Te-Se	Γ @ VB	(10.6,0.9,0.2)	(157.7,180.0,-53.0)	(7.9,1.6,0.5)	(13.0,2.0,-11.0)	-0.02	0.0	0.0	0.0	T @ AB
		K @ CB	(10.6,0.9,0.2)	(157.7,180.0,-53.0)	(6.6,0.5,0.8)	(75.5,51.9,-41.5)	4.7	0.07	20.9	0.0	T @ AB

As an example, in Fig. 2 the band structure of AA and MX stacked WSSe is shown for the three possible orderings. In WSSe bilayers with the Se-S-Se-S interface configuration, named only by the chalcogen planes, there is an obvious layer polarization caused by the intrinsic dipole moment of the layers and the asymmetry of the order. At the interface, the potential energy on the side of the S atomic plane is larger, so the energy of the top layer is larger than in the other layer. Since the layers are weakly coupled, this results in the bottom (top) layer contributing to the CBM (VBM).

On the contrary, in bilayers with symmetric orders (S-Se-Se-S and Se-S-S-Se), the effective dipole in each layer points in opposite directions and the VBM/CBM combine states from both layers. Therefore, the electronic structure of twisted Janus TMDs bilayers and their consequent physical properties will sensitively depend not only on the chemical compositions, but also on the interface orderings.

A. Twisted bilayers moiré Hamiltonian

We derive the moiré Hamiltonian from first principles following the approach outlined in Ref. [60]. The procedure requires a relatively inexpensive set of bilayer untwisted calculations. These calculations are intended to extract how the Bloch states near a band edge are affected by the misalignment between the layers. This information is then used to derive a continuum model Hamiltonian which targets the moiré bands that form in twisted bilayers. This model is further augmented to include lattice relaxation [61], an effective mass correction, and Rashba spin-orbit coupling terms.

For twisted semiconductors, the moiré bands closest to the band gap can be derived from the untwisted parabolic band extrema (or valleys) in the original Brillouin zone. In particular, in Janus bilayers, we can identify two distinct situations.

In the first one, when the two layers are dissimilar or weakly coupled, the moiré physics derives mostly from one layer only. This condition is not relevant only for heterobilayers, but also for asymmetrically ordered homobilayers (X-Y-X-Y). In this case, the bilayer's effective dipole shifts in energy each layer's band edge, so that the VBM/CBM are mostly layer polarized states.

A different second situation is that of symmetrically ordered homobilayers (X-Y-Y-X or Y-X-X-Y), where the system recovers the mirror symmetry that relates the chalcogen planes, so that the layer's effective dipoles cancel out. This further implies they are D_3 centrosymmetric structures in which Rashba spin splittings are forbidden by symmetry. Therefore the main differences between asymmetrically ordered homobilayers or heterobilayers and symmetrically ordered homobilayers are the presence or not of Rashba effects and the degree of layer polarization.

In momentum space, the valence band maximum is located either at the Brillouin zone corners (K/K') or at Γ. In the former case with the VBM at K/K', the strong Ising spin-orbit splitting isolates in energy one state per valley, realizing a situation similar to that of nonpolar TMD heterobilayers [39].

In the latter case with the VBM at Γ, the interlayer interaction is particularly important, as out-of-plane d_{z^2}/p_z orbitals are involved at the band edge. This leads to a large band splitting where the VBM is the layer antibonding state that, depending on the degree of layer polarization, is separated by

TABLE III. Heterobilayer continuum model parameters. All symbols have the same meaning as in Table II. For each material there are now three lines, corresponding to the values for the respective band edges: Γ at the VBM, K at the VBM, and K at the CBM.

Material	Stack ordering	Band Edge	$W_{1,2,3}$	$\phi_W^{1,2,3}$	$V_{1,2,3}$	$\phi_V^{1,2,3}$	m_0^*	U_1	ϕ_U^1	α_R	MSL
3R MoSSe/WSSe	S-Se-S-Se	Γ @ VB	(7.4,1.5,0.6)	(-3.7,177.9, 54.6)	(5.3,6.6,2.8)	(121.3,3.8,-125.6)	-0.6	0.02	-20.5	25.4	T @ XM
		K @ VB	(7.4,1.5,0.6)	(-3.7,177.9, 54.6)	(3.7,0.6,0.4)	(104.6,166.0,-99.5)	-2.3	0.01	-2.3	0.0	T @ XM
		K @ CB	(7.4,1.5,0.6)	(-3.7,177.9, 54.6)	(3.6,0.3,0.8)	(-106.2, -157.9, 61.5)	2.1	0.02	-173.0	0.0	T @ XM
	S-Se-Se-S	Γ @ VB	(11.5,0.7,0.6)	(146.2, -167.0, -61.9)	(9.3, 5.2, 1.7)	(-165.8, 1.8, -2.4)	-0.75	0.0	0.0	60.8	T @ MX
		K @ VB	(11.5,0.7,0.6)	(146.2, -167.0, -61.9)	(4.0,0.5,1.0)	(-61.7,13.9,24.2)	-2.7	0.0	0.0	0.0	T @ MX
		K @ VB	(11.5,0.7,0.6)	(146.2, -167.0, -61.9)	(2.5,0.3,0.8)	(108.1,0.3,-23.0)	1.6	0.03	-12.9	0.0	T @ MX
	Se-S-S-Se	Γ @ VB	(10.0,2.1,0.9)	(-0.7,180.0,179.2)	(38.3,14.8,11.1)	(-178.9,0.7,0.8)	-1.0	0.1	0.0	44.5	T @ MX
		K @ VB	(10.0,2.1,0.9)	(-0.7,180.0,179.2)	(8.1,0.8,1.6)	(-59.9,180.0,140.4)	-2.68	0.0	0.0	0.0	T @ MX
		K @ CB	(10.0,2.1,0.9)	(-0.7,180.0,179.2)	(6.2,0.0,1.1)	(81.8,-164.0,-129.4)	1.8	0.01	0.0	0.0	T @ MX
	Se-S-Se-S	Γ @ VB	(9.7, 2.1, 0.7)	(-5.3, -179.9, 162.1)	(9.3, 5.2, 1.7)	(-165.8, 1.8, -2.4)	-0.75	0.0	0.0	60.8	T @ MX
		K @ VB	(9.7, 2.1, 0.7)	(-5.3, -179.9, 162.1)	(8.0,2.4,1.9)	(-54.5,180.0,141.4)	-2.7	0.0	0.0	0.0	T @ MX
		K @ CB	(9.7, 2.1, 0.7)	(-5.3, -179.9, 162.1)	(6.0,1.1,1.0)	(113.4,-3.9,-90.4)	1.8	0.01	-4.4	0.0	T @ MX
2H MoSSe/WSSe	S-Se-S-Se	Γ @ VB	(4.8, 0.1, 0.1)	(132.1, 0.5, -78.1)	(2.8, 0.1, 0.2)	(116.9, 22.2, -102.9)	-0.55	0.0	0.0	29.8	T @ XX
		K @ VB	(4.8, 0.1, 0.1)	(132.1, 0.5, -78.1)	(0.8, 0.1, 0.2)	(-26.4, 97.8, -70.6)	-2.28	0.0	0.0	0.0	T @ AB
		K @ CB	(4.8, 0.1, 0.1)	(132.1, 0.5, -78.1)	(1.2, 0.0, 0.1)	(-70.9, -28.5, 109.7)	-2.06	0.0	0.0	0.0	T @ MM
	S-Se-Se-S	Γ @ VB	(7.9, 1.3, 0.6)	(143.7, 179.7, 123.6)	(8.9, 1.8, 2.9)	(-26.5, -0.6, -3.9)	-1.04	0.0	0.0	64.5	T @ AB
		K @ VB	(7.9, 1.3, 0.6)	(143.7, 179.7, 123.6)	(0.8, 0.1, 0.2)	(-26.4, 97.8, -70.6)	-2.28	0.0	0.0	0.0	T @ AB
		K @ CB	(7.9, 1.3, 0.6)	(143.7, 179.7, 123.6)	(1.2, 0.0, 0.1)	(-70.9, -28.5, 109.7)	-2.06	0.0	0.0	0.0	T @ MM
	Se-S-S-Se	Γ @ VB	(3.3, 0.1, 0.3)	(129.1, 27.8, -10.7)	(4.9, 0.3, 0.2)	(123.2, -76.4, -122.0)	-0.73	0.0	0.0	67.1	T @ MM
		K @ VB	(3.3, 0.1, 0.3)	(129.1, 27.8, -10.7)	(0.8, 0.1, 0.2)	(-26.4, 97.8, -70.6)	-2.28	0.0	0.0	0.0	T @ AB
		K @ CB	(3.3, 0.1, 0.3)	(129.1, 27.8, -10.7)	(1.2, 0.0, 0.1)	(-70.9, -28.5, 109.7)	-2.06	0.0	0.0	0.0	T @ MM
	Se-S-Se-S	Γ @ VB	(8.3, 1.8, 0.7)	(137.1, 180.0, 34.5)	(6.8, 5.0, 2.4)	(-32.8, -0.9, -145.8)	-0.69	0.0	0.0	70.1	T @ XX
		K @ VB	(8.3, 1.8, 0.7)	(137.1, 180.0, 34.5)	(0.8, 0.1, 0.2)	(-26.4, 97.8, -70.6)	-2.28	0.0	0.0	0.0	T @ AB
		K @ CB	(8.3, 1.8, 0.7)	(137.1, 180.0, 34.5)	(1.2, 0.0, 0.1)	(-70.9, -28.5, 109.7)	-2.06	0.0	0.0	0.0	T @ XX
3R MoSTe/WSTe	S-Te-S-Te	Γ @ VB	(10.6, 2.0, 0.7)	(8.3, 180.0, -150.6)	(5.1, 0.9, 2.0)	(-164.6, 172.5, 175.9)	-0.65	0.02	-4.5	68.1	T @ MX
		K @ VB	(10.6, 2.0, 0.7)	(8.3, 180.0, -150.6)	(4.9, 0.3, 1.0)	(42.4, -24.0, -52.8)	-1.83	0.01	-70.0	0.0	T @ AA
		K @ CB	(10.6, 2.0, 0.7)	(8.3, 180.0, -150.6)	(3.5, 0.4, 0.8)	(-6.6, 27.5, -0.5)	1.64	0.02	25.4	0.0	T @ XM
	S-Te-Te-S	Γ @ VB	(9.6, 1.8, 0.5)	(0.0, 180.0, 176.6)	(2.4, 0.5, 0.1)	(-12.7, 1.9, 20.9)	-0.55	0.01	180.0	186.4	T @ MX
		K @ VB	(9.6, 1.8, 0.5)	(0.0, 180.0, 176.6)	(7.2, 0.5, 0.7)	(-37.4, 161.2, 66.6)	-2.1	0.01	166.0	0.0	T @ MX
		K @ CB	(9.6, 1.8, 0.5)	(0.0, 180.0, 176.6)	(2.3, 0.3, 0.15)	(11.9, -180.0, -12.6)	0.6	0.07	-3.0	0.0	T @ MX
	Te-S-S-Te	Γ @ VB	(12.5, 2.5, 1.0)	(-0.3, 180.0, 180.0)	(29.0, 4.3, 2.6)	(-177.4, 2.1, -3.5)	-1.6	0.15	0.0	32.6	T @ MX
		K @ VB	(12.5, 2.5, 1.0)	(0.4, 180.0, 180.0)	(13.6, 0.5, 1.0)	(-31.4, -166.3, 123.6)	-2.13	0.01	130.0	0.0	T @ MX
		K @ CB	(12.5, 2.5, 1.0)	(0.4, 180.0, 180.0)	(10.4, 1.8, 1.1)	(44.7, 2.5, -74.7)	1.15	0.01	28.5	0.0	T @ MX
	Te-S-Te-S	Γ @ VB	(10.6, 2.0, 0.7)	(8.1, 180.0, -151.7)	(5.1, 0.9, 2.0)	(-166.8, 175.0, 175.8)	-0.65	0.02	-4.9	69.1	T @ MX
		K @ VB	(10.6, 2.0, 0.7)	(8.1, 180.0, -151.7)	(3.2, 0.9, 1.3)	(-66.4, 0.0, 31.33)	-2.1	0.01	55.2	0.0	T @ MX
		K @ CB	(10.6, 2.0, 0.7)	(8.1, 180.0, -151.7)	(3.9, 0.3, 0.95)	(2.7, -22.5, -13.7)	1.1	0.02	55.3	0.0	T @ MX
2H MoSTe/WSTe	S-Te-S-Te	Γ @ VB	(10.1, 1.1, 0.9)	(132.3, 180.0, 61.6)	(1.8, 0.9, 0.9)	(55.0, -4.1, -102.1)	-0.4	0.0	0.0	98.9	T @ MM
		K @ VB	(10.1, 1.1, 0.9)	(132.3, 180.0, 61.6)	(0.5,1.5, 1.0)	(-73.3, 1.4, -103.6)	-1.83	0.01	43.3	0.0	T @ XX
		K @ CB	(10.1, 1.1, 0.9)	(132.3, 180.0, 61.6)	(1.1, 0.7, 0.5)	(-118.6, 31.5, -142.9)	1.66	0.03	24.0	0.0	T @ MM
	S-Te-Te-S	Γ @ VB	(9.7, 1.6, 0.8)	(153.3, 180.0, 130.6)	(3.0, 0.5, 0.2)	(134.6, 1.2, -19.5)	-0.55	0.01	160.0	227.4	T @ XX
		K @ VB	(9.7, 1.6, 0.8)	(153.3, 180.0, 130.6)	(7.1, 0.7, 0.9)	(-36.4, 171.2, 81.6)	-2.1	0.01	166.0	0.0	T @ MM
		K @ CB	(9.7, 1.6, 0.8)	(153.3, 180.0, 130.6)	(2.3, 0.3, 0.15)	(11.9, -180.0, -12.6)	0.6	0.07	-3.0	0.0	T @ MM
	Te-S-S-Te	Γ @ VB	(10.9, 1.7, 0.9)	(117.3, 178.0, 46.6)	(29.0, 5.7, 3.6)	(-177.4, 1.0, -2.3)	-1.6	0.15	0.0	32.6	T @ MM
		K @ VB	(10.9, 1.7, 0.9)	(117.3, 178.0, 46.6)	(9.6, 0.3, 1.5)	(98.0, -113.5, -47.1)	-2.14	0.0	0.0	0.0	T @ XX
		K @ CB	(10.9, 1.7, 0.9)	(117.3, 178.0, 46.6)	(4.1, 1.4, 0.2)	(115.0, -9.4, 60.2)	1.14	0.01	71.6	0.0	T @ MM
	Te-S-Te-S	Γ @ VB	(9.9, 1.8, 0.7)	(137.3, 180.0, 100.6)	(27.8, 20.5, 13.7)	(-1.8, -33.0, 8.7)	-0.65	0.02	-6.1	69.8	T @ AB
		K @ VB	(9.9, 1.8, 0.7)	(137.3, 180.0, 100.6)	(5.0, 0.2, 1.3)	(167.0, -171.0, -157.8)	-2.1	0.01	56.2	0.0	T @ XX
		K @ CB	(9.9, 1.8, 0.7)	(137.3, 180.0, 100.6)	(2.5, 0.4, 1.1)	(140.9, 1.5, -143.7)	1.1	0.02	-33.8	0.0	T @ AB

its bonding counterpart by several tens or hundreds of meV. When Rashba SOC vanishes due to symmetry, the physics is then similar to that of nonpolar TMD homobilayers [40] where the Γ band edge is spin degenerate.

The conduction band minimum is either at K/K' or the Q points [62]. The physics of the moiré bands forming around the Q points will be discussed in future work.

1. Continuum model Hamiltonian

The low-energy physics of twisted hetero/homobilayers can be modeled by means of a low-energy continuum model Hamiltonian. In both symmetrically and asymmetrically ordered twisted bilayers, the conduction and valence band edges are isolated in energy by at least 50–100 meV.

TABLE III. (*continued.*)

| Material	Stack ordering	Band Edge	$W_{1,2,3}$	$\phi_W^{1,2,3}$	$V_{1,2,3}$	$\phi_V^{1,2,3}$	m_0^*	U_1	ϕ_U^1	α_R	MSL
3R MoSeTe/WSeTe	Se-Te-Se-Te	Γ @ VB	(13.3, 2.4, 0.9)	(2.3, 180.0, -170.0)	(16.9, 2.2, 1.6)	(3.4, 142.5, 176.7)	-0.7	0.04	11.1	109.0	T @ XM
		K @ VB	(13.3, 2.4, 0.9)	(2.3, 180.0, -170.0)	(12.6, 2.2, 0.7)	(82.3, -5.6, -39.6)	-2.0	0.0	0.0	0.0	T @ XM
		K @ CB	(13.3, 2.4, 0.9)	(2.3, 180.0, -170.0)	(2.6, 1.8, 0.6)	(-17.8, 2.8, 5.0)	1.9	0.03	4.9	0.0	T @ XM
	Se-Te-Te-Se	Γ @ VB	(12.0, 2.2, 0.7)	(-0.5, 180.0, -178.6)	(22.2, 16.2, 9.9)	(-3.7, -26.9, -4.6)	-0.7	0.01	-7.4	70.9	T @ AA
		K @ VB	(12.0, 2.2, 0.7)	(-0.5, 180.0, -178.6)	(10.8, 0.6, 0.9)	(-34.4, 164.2, 99.6)	-2.35	0.01	151.0	0.0	T @ AA
		K @ CB	(12.0, 2.2, 0.7)	(-0.5, 180.0, -178.6)	(6.9, 0.6, 0.4)	(21.1, -177.0, -162.6)	1.0	0.06	-11.0	0.0	T @ MX
	Te-Se-Se-Te	Γ @ VB	(15.3, 2.4, 1.0)	(0.0, 180.0, 180.0)	(14.9, 5.2, 5.6)	(170.0, 142.5, 176.7)	-0.7	0.03	3.1	73.0	T @ AA
		K @ VB	(15.3, 2.4, 1.0)	(0.0, 180.0, 180.0)	(10.4, 0.9, 0.2)	(-53.3, 148.6, 16.6)	-2.4	0.01	141.7	0.0	T @ AA
		K @ CB	(15.3, 2.4, 1.0)	(0.0, 180.0, 180.0)	(9.9, 1.5, 1.1)	(60.6, 180.0, -70.0)	1.57	0.01	20.0	0.0	T @ XM
	Te-Se-Te-Se	Γ @ VB	(15.3, 3.5, 0.9)	(-2.1, 180.0, 168.7)	(17.1, 7.9, 2.0)	(-3.0, 5.0, 5.8)	-0.65	0.01	-8.9	72.1	T @AA
		K @ VB	(15.3, 3.5, 0.9)	(-2.1, 180.0, 168.7)	(7.5, 1.1, 0.3)	(135.4, 0.5, 20.33)	-2.4	0.0	0.0	0.0	T @ XM
		K @ CB	(15.3, 3.5, 0.9)	(-2.1, 180.0, 168.7)	(8.0, 1.3, 0.3)	(134.7, 0.5, -4.7)	1.5	0.02	-32.3	0.0	T @ AA
2H MoSeTe/WSeTe	Se-Te-Se-Te	Γ @ VB	(13.4, 2.3, 0.9)	(2.3, 180.0, -169.0)	(16.9, 2.2, 1.6)	(3.4, 142.5, 176.7)	-0.7	0.04	11.1	109.0	T @ XX
		K @ VB	(13.4, 2.3, 0.9)	(2.3, 180.0, -169.0)	(12.6, 2.2, 0.7)	(82.3, -5.6, -39.6)	-2.0	0.0	0.0	0.0	T @ XX
		K @ CB	(13.4, 2.3, 0.9)	(2.3, 180.0, -169.0)	(2.6, 1.8, 0.6)	(-17.8, 2.8, 5.0)	1.9	0.03	4.9	0.0	T @ XX
	Se-Te-Te-Se	Γ @ VB	(12.0, 2.0, 0.9)	(148.6, 180.0, 122.5)	(3.3, 2.4, 1.4)	(25.6, 2.0, -40.6)	-1.24	0.04	155.4	29.0	T @ AB
		K @ VB	(12.0, 2.0, 0.9)	(148.6, 180.0, 122.5)	(8.0, 0.1, 0.3)	(148.7, 164.9, -55.6)	-2.36	0.01	23.0	0.0	T @ XX
		K @ CB	(12.0, 2.0, 0.9)	(148.6, 180.0, 122.5)	(5.3, 0.1, 0.4)	(132.9, 30.9, 4.2)	1.0	0.07	164.0	0.0	T @ AB
	Te-Se-Se-Te	Γ @ VB	(9.9, 2.0, 0.8)	(126.0, 180.0, 51.2)	(25.7, 6.6, 5.1)	(-62.8, -4.8, 164.7)	-0.9	0.1	127.1	65.5	T @ MM
		K @ VB	(9.9, 2.0, 0.8)	(126.0, 180.0, 51.2)	(4.5, 0.4, 0.4)	(130.3, 145.6, -16.2)	-2.4	0.01	107.7	0.0	T @ XX
		K @ CB	(9.9, 2.0, 0.8)	(126.0, 180.0, 51.2)	(2.6, 0.2, 0.4)	(127.6, -2.7, -58.0)	1.44	0.01	67.0	0.0	T @ MM
	Te-Se-Te-Se	Γ @ VB	(12.0, 3.0, 1.8)	(135.8, 180.0, 59.8)	(2.1, 1.3, 0.5)	(21.7, 172.0, 55.8)	-0.61	0.03	120.3	153.0	T @ XX
		K @ VB	(12.0, 3.0, 1.8)	(135.8, 180.0, 59.8)	(7.4, 4.2, 2.3)	(112.4, 3.2, -166.3)	-2.4	0.01	46.9	0.0	T @ XX
		K @ CB	(12.0, 3.0, 1.8)	(135.8, 180.0, 59.8)	(4.5, 1.4, 1.2)	(160.7, -3.3, -82.7)	1.45	0.02	94.0	0.0	T @ AB
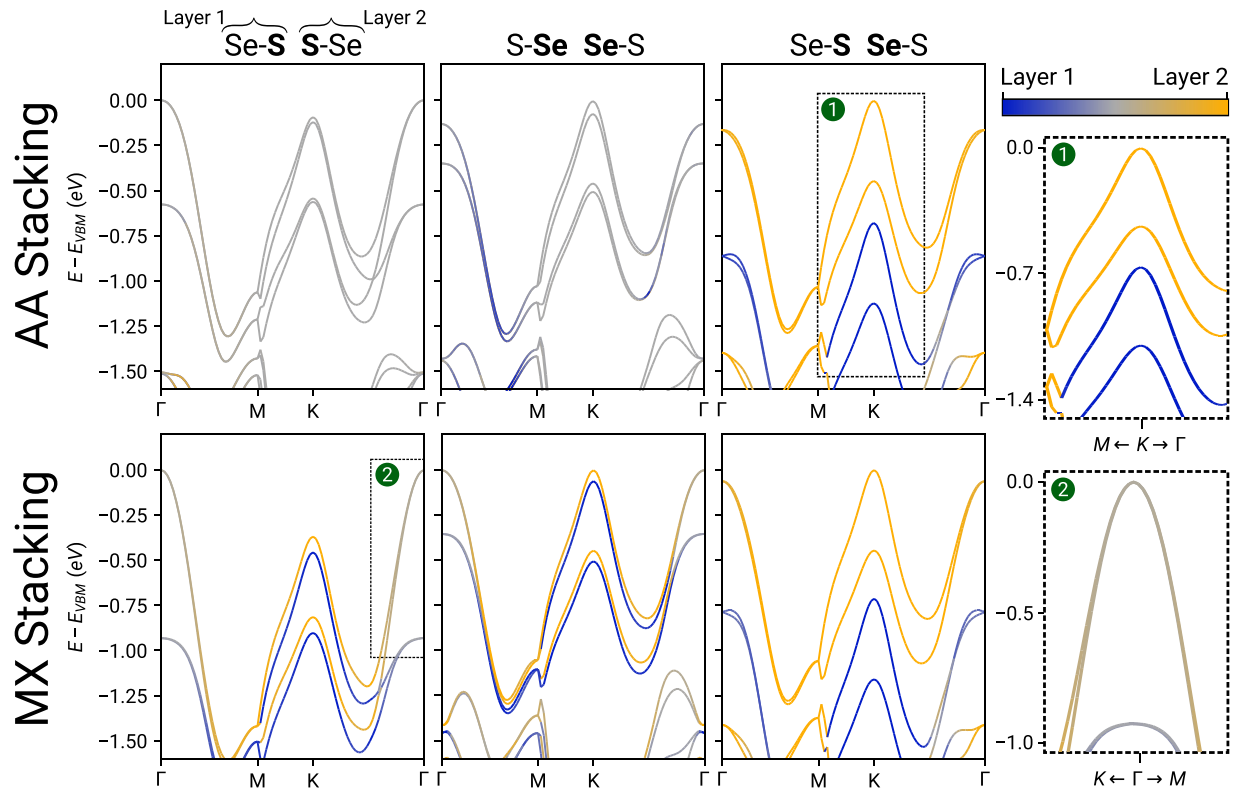
FIG. 2. Homobilayer band structures of WSSe at different stackings, projected on each monolayer (blue to orange). The energy is shifted to the valence band maximum of each configuration. Inset 1 highlights the K valley of an asymmetrically ordered bilayer (Se-S-Se-S), presenting both maximal layer polarization and strong spin-orbit spin splitting. Inset 2 highlights the Γ-valley of a symmetrically ordered bilayer (Se-S-S-Se), where strong interlayer interaction, especially between p_z and d_{z^2} orbitals, leads to a large band splitting, isolating the valence band maximum (antibonding state) from other states.

The corresponding moiré physics is well described by the one-band continuum model Hamiltonian [39,40]:

$$\mathcal{H} = -\frac{\hbar^2 \mathbf{k}^2}{2m_0^*} + \Delta(\mathbf{r}) + \varepsilon_{m^*}(\mathbf{r}) - \alpha_R(\boldsymbol{\sigma} \times \mathbf{k}) \cdot \hat{z}, \quad (1)$$

where m_0^* and α_R are the average (over all the stacking configurations) effective mass and Rashba parameter, $\Delta(\mathbf{r})$ is the moiré potential, $\varepsilon_{m^*}(\mathbf{r})$ is the effective mass correction, $\mathbf{r}$ tracks the local stacking configuration, and $\boldsymbol{\sigma}$ are Pauli matrices.

$\Delta(\mathbf{r})$ and $\varepsilon_{m^*}(\mathbf{r})$ are scalar functions that capture the energy and effective mass of holes/electrons in the VBM/CBM as a function of the relative in-plane displacement $\mathbf{r}$ between the two aligned layers. To capture the stacking-dependent electronic details necessary for the determination of these potentials, we perform density functional theory (DFT) calculations on nontwisted bilayers. Accordingly, we refer to this model as a first-principles effective Hamiltonian. The DFT calculations are performed with the aim of sampling how the physics locally changes with stacking: the top layer is shifted relative to the bottom layer over a 9×9 grid in the unit cell.

These calculations are performed with QUANTUM ESPRESSO [63,64] using the generalized gradient approximation with the weak vdW forces acting between the layers taken into account by the nonlocal vdW functional vdW-DF2-C09 [65,66]. All calculations include spin-orbit coupling. For each displacement, the in-plane position of the atoms is fixed while the interlayer distance is relaxed. The total energy, band edge energy, and effective mass are extracted for each bilayer stacking and then used in the continuum model. To find the effective mass and Rashba coupling, we fit the values obtained from the aligned bilayer band edges to the $\varepsilon\mathbf{k}^2 + \alpha|\mathbf{k}|$ function. The quadratic term tracks the effective mass ε, while the linear term takes into account the Rashba spin splitting α. In general, we found that, unlike for the effective mass, α is only weakly dependent on stacking. We therefore consider in the continuum model only the average (over stacking configurations) Rashba parameter α_R. In the Supplemental Material Fig. S1 [67], we validate the continuum model against explicit large-scale DFT calculations and corroborate the good agreement near the band extremum.

2. Lattice relaxation

To evaluate in-plane relaxation effects, we first compute the monolayer bulk and shear moduli $\mathcal{G}$ and $\mathcal{K}$ (see Table I). For the interlayer energy, we extract from the bilayer's DFT calculations their total energies, which are then combined in the generalized stacking fault energy functional (GSFE) $\Omega(\mathbf{r})$ [61,68,69]. The GSFE tracks how the interlayer energy depends on the relative stacking between the layers.

We then minimize the total mechanical energy of the moiré pattern, obtaining the top/bottom layer relaxation displacements $\mathbf{u}_{t/b}$. In general, the relaxation distorts the layers to maximize the area of the lowest-energy stacking between layers. This is achieved via small in-plane deformations characterized by strain fields that locally change the layer alignment [23,61]. Out-of-plane relaxation is implicitly included at the level of the DFT calculations, with each stacking allowed to move to its ideal interlayer separation.

Finally, we incorporate the effect of atomic relaxations on the electronic Hamiltonian of Eq. (1) through a linear mapping that updates the unrelaxed configuration $\mathbf{r} \to \mathbf{r} + \mathbf{u}_t + \mathbf{u}_b$ [70]. The relaxed GSFE of several twisted bilayers is shown in the Supplemental Material [67].

3. Fourier expansion

The two-dimensional periodicity of the aligned bilayers implies that the potentials $\Delta(\mathbf{r})$, $\varepsilon_{m^*}(\mathbf{r})$, and $\Omega(\mathbf{r})$ are periodic functions that can be Fourier transformed in momentum space. All the information relative to the moiré pattern, from its structural relaxation to its effect on the bilayer effective masses, is therefore conveniently stored in few Fourier coefficients.

The number of these coefficients can be reduced by taking into account symmetry. Threefold rotations with respect to the out-of-plane z axis (C_{3z}) require that the potentials and their Fourier transforms are invariant under $120°$ rotations. This, and the fact that the potentials are real functions, reduces the number of independent coefficients to two: an amplitude and phase ϕ [39,40].

Therefore the potentials can be expressed as follows:

$$\Omega(\mathbf{r}) = \sum_{l=1}^{3} \sum_{j=1}^{6} W_l \exp\left(i\mathbf{g}_j^l \cdot \mathbf{r} + \phi_W^l\right), \quad (2a)$$

$$\Delta(\mathbf{r}) = \sum_{l=1}^{3} \sum_{j=1}^{6} V_l \exp\left(i\mathbf{g}_j^l \cdot \mathbf{r} + \phi_V^l\right), \quad (2b)$$

$$\varepsilon(\mathbf{r}) = \sum_{j=1}^{6} U_1 \exp\left(i\mathbf{g}_j^1 \cdot \mathbf{r} + \phi_U^1\right), \quad (2c)$$

where $\mathbf{g}_{j+1}^l = C_{6z}\mathbf{g}_j^l$ is the lth shell of six moiré $\mathbf{g}$ vectors ordered with increasing $|\mathbf{g}|$. Unlike for the effective mass correction, the moiré potential and GSFE have to be expanded up to the third momentum shell to accurately capture the moiré physics.

B. Moiré bands without Rashba effects: Symmetric homobilayers and emergent symmetries

We start by focusing on symmetrically ordered homobilayers (X-Y-Y-X or Y-X-X-Y). In these cases the system recovers the mirror symmetry that relates the chalcogen planes. Being centrosymmetric structures, Rashba spin splittings are forbidden by symmetry.

We consider a simplified version of the Hamiltonian in Eq. (1) and solve for the Bloch states by expanding in plane waves:

$$\begin{aligned}
\langle \mathbf{k} + \mathbf{g}'|\mathcal{H}|\mathbf{k} + \mathbf{g}\rangle \\
= -\delta_{\mathbf{g},\mathbf{g}'}\frac{\hbar^2|\mathbf{k} + \mathbf{g}|^2}{2m_0^*} + \Delta(\mathbf{g} - \mathbf{g}') + \varepsilon(\mathbf{g} - \mathbf{g}'), \quad (3)
\end{aligned}$$

where $\mathbf{k}$ is a wave vector in the moiré Brillouin zone. We then use the continuum model to calculate the band structure of twisted Janus TMDs at angles where full microscopic calculations are prohibitive.
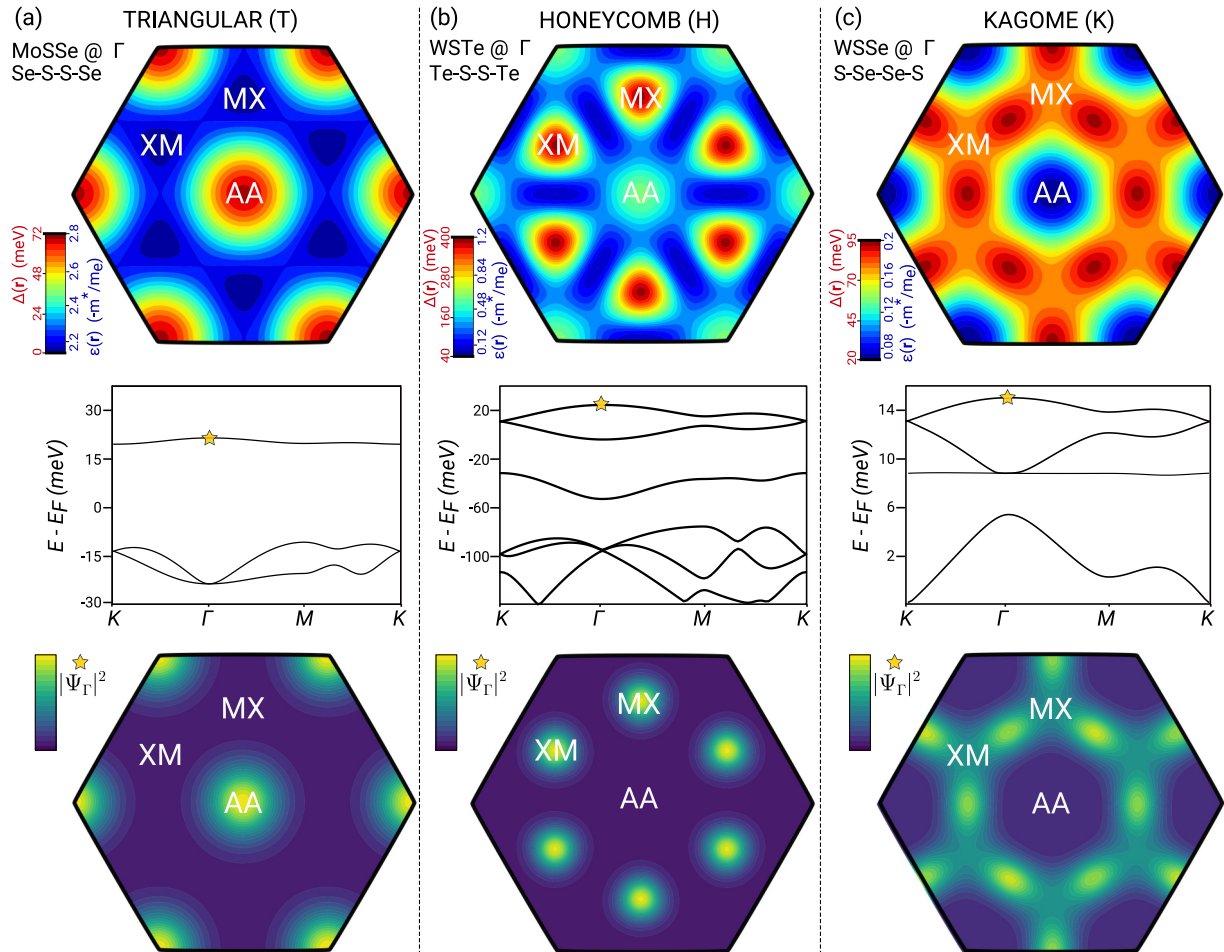
FIG. 3. Continuum model moiré and effective mass potentials, band structure, and charge density distribution are shown for three representative examples, each displaying the different possible physics of twisted Janus TMDs. The examples are (a) 3R MoSSe, (b) 3R WSTe, and (c) 3R WSSe twisted homobilayers with twist angles 4.0°, 3.0°, and 1.5°, respectively. The moiré $\Delta(\mathbf{r})$ and effective mass potential $\varepsilon(\mathbf{r})$ follow the same real space distribution (encoded in colors). The charge distribution of the topmost Bloch state (denoted by a star) is shown. The charge is localized around the highly symmetric moiré potential maxima that form, in each example, triangular, honeycomb, and kagome networks. In the last column of Tables II and III, we present the characterization of each system in terms of which moiré superlattice it forms, along with the corresponding continuum model parameters.

1. Emergent symmetries

An interesting feature of moiré materials is that the potentials in Eq. (2) can develop symmetries additional to those of the underlying twisted lattice, with profound consequences on the electronic and elastic properties of the system [23,25,40,71,72]. In symmetrically ordered 3R bilayers with D_3 symmetry, two bilayers stacked by $\mathbf{r}$ and $C_{2z}\mathbf{r} = -\mathbf{r}$ are mapped into each other by a $z \leftrightarrow -z$ mirror operation and hence have the same band and total energies. This property, which is peculiar to 3R homobilayers, further implies that $\Delta(\mathbf{r}) = \Delta(C_{2z}\mathbf{r})$, $\varepsilon_{m^*}(\mathbf{r}) = \varepsilon_{m^*}(C_{2z}\mathbf{r})$, and $\Omega(\mathbf{r}) = \Omega(C_{2z}(\mathbf{r}))$, i.e., that the potentials are inversion-symmetric functions. In terms of their expansion in momentum space, this constrains the phases ϕ in Eq. (2) to be either 0 or π [40].

The moiré Hamiltonian in Eq. (1) and the GSFE inherit this additional symmetry. This, combined with the threefold rotations, promotes them to be sixfold (D_6) symmetric functions. This allows the moiré band structure to have distinct features, such as Dirac nodes, which would otherwise be forbidden by symmetry.

It is important to stress that the moiré Hamiltonian in Eq. (1) and also the GSFE develop the emergent C_{2z} symmetry of the group D_6, despite the lattice having only threefold D_3 symmetry.

2. Band structure symmetry analysis

We employ the topological quantum chemistry theory [73] to identify the symmetries and centers of the Wannier orbitals underlying the moiré bands. This procedure involves computing the symmetry of the Bloch states, classifying them in terms of the irreducible representations (irreps) of the little groups at the corresponding high-symmetry points, and then comparing the list of irreps with the elementary band representations (EBRs) listed on the Bilbao Crystallographic server [74]. The centers of the Wannier orbitals for all the twisted bilayers' considered are listed in Tables II and III.

In Fig. 3 the valence band structure of three different twisted bilayers is shown along with their moiré/effective mass potentials and charge distribution. They are three representative examples of the different physics that can occur

in twisted Janus TMDs. As can be seen, the maxima of the potentials are located around high-symmetry regions of the moiré pattern. As a consequence, the charge tends to localize around these maxima, as shown by the charge distribution of the topmost moiré bands.

Thus, the moiré pattern acts as a long-wavelength confining potential, localizing holes/electrons around triangular, honeycomb, and kagome lattice sites. This behavior can be understood [39,40,61] by making a harmonic approximation to the moiré potential near its minima/maxima, thus identifying the harmonic oscillator wave functions as Wannier functions. The Bloch state symmetry analysis agrees with this picture. The Wannier orbitals generating the topmost set of moiré bands transform as a fully symmetric s state, while the set of bands below is spanned by $p_x \pm i p_y$.

Thus, Fig. 3 summarizes the richness of the physics found in TMD Janus homobilayers, and in Table II we present the characterization of each system in terms of which moiré superlattice it forms, along with the corresponding continuum model parameters. Depending on the valley, chalcogen ordering, 3R/2H twist configuration, and chemical composition, the system realizes a platform to simulate triangular, honeycomb, and kagome flat bands, respectively, shown in Figs. 3(a)–3(c). The first case is usual and commonly known for twisted hexagonal systems, including TMDs. The last two cases are a peculiarity of 3R symmetrically ordered twisted bilayers and the emergent sixfold symmetry of the continuum model Hamiltonian. In particular, in Fig. 3(b) the charge localizes around the honeycomb network formed by the MX/XM regions. The topmost set of bands is nondegenerate at Γ, forms a Dirac node at K, and is topologically equivalent to the π bands of graphene. The bands in Fig. 3(c) are even more intriguing, as they exhibit an extremely narrow band degenerate at Γ and Dirac nodes. These bands are those of the geometrically frustrated kagome lattice, an exotic situation that can host interesting correlated phenomena such as magnetic frustration and spin liquid physics [75,76]. The charge distribution, which is localized around the kagome network formed by the domain wall centers, further confirms this picture.

C. Moiré bands with Rashba effects: Asymmetric homobilayers and heterobilayers

We now discuss the physics of heterobilayers and asymmetrically ordered homobilayers. In these cases, due to the dissimilarity between the layers or chalcogen ordering, the system is noncentrosymmetric. This further implies that Rashba SOC is not prevented to arise around the valence band edge at Γ. By expanding in plane waves the full Hamiltonian in Eq. (1), we obtain

$$\langle \mathbf{k}+\mathbf{g}, s|\mathcal{H}|\mathbf{k}+\mathbf{g}', s'\rangle$$
$$= -\delta_{\mathbf{g},\mathbf{g}'}\delta_{\mathbf{s},\mathbf{s}'}\frac{\hbar^2|\mathbf{k}+\mathbf{g}|^2}{2m_0^*} + \delta_{\mathbf{s},\mathbf{s}'}\Delta(\mathbf{g}-\mathbf{g}')$$
$$+ \delta_{\mathbf{s},\mathbf{s}'}\varepsilon(\mathbf{g}-\mathbf{g}') + \delta_{\mathbf{g},\mathbf{g}'}\alpha_R[(k_y+g_y)\sigma_x-(k_x+g_x)\sigma_y], \quad (4)$$

where s is the spin index, $\sigma_{x,y,z}$ are Pauli matrices, and otherwise the same notation as before.

In Fig. 4 we show the spin-resolved band structure of a MoSSe/WSSe heterobilayer twisted at 3 degrees (more ex-
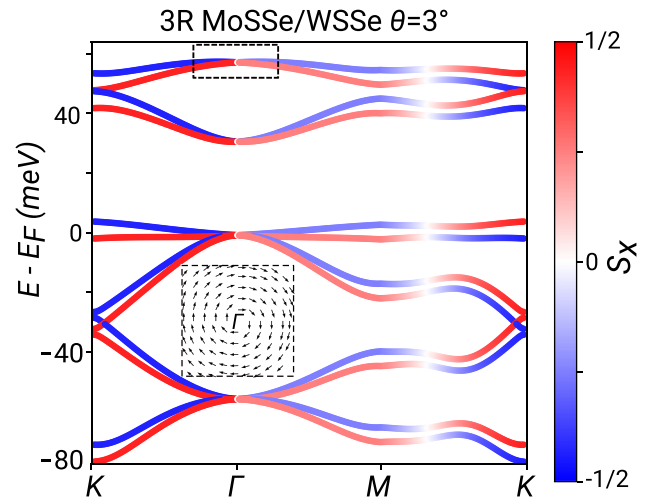

FIG. 4. Γ-valley moiré valence bands of 3R MoSSe/WSSe with Se-S-S-Se ordering, at $\theta = 3°$. The S_x spin component is encoded in colors. The in-plane spin texture of the Bloch states around Γ in the topmost moiré band is shown in the inset. The spin distribution in momentum space follows a spiral pattern winding around Γ.

amples are shown in the Supplemental Material [67]). Given the 3R configuration and the symmetry of chalcogen layer ordering, the band-structure resembles that of the honeycomb network moiré materials [Fig. 3(b)], with the first set of bands similar to that of graphene. The second set of four bands resembles that of $p_x \pm i p_y$ orbitals on a honeycomb lattice. However, in heterobilayers, the fourfold Dirac degeneracy at the K points is lifted. First of all, the moiré potential is not sixfold symmetric because the MX regions, with a molybdenum atom on top of a pair of chalcogens, has a slightly different energy than the XM regions, where the chalcogens are on top of a tungsten atom. The imbalance between the MX/XM honeycomb lattice sites corresponds to a mass term in the Dirac Hamiltonian [77]. On top of this, the Rashba spin-orbit coupling further spoils the Dirac nodes by lifting the spin degeneracy. The spin texture distribution in momentum space follows a spiral pattern winding around Γ.

The continuum model parameters for the Janus TMDs heterobilayers, all having triangular moiré superlattices, are listed in Table III, while the parameters for the asymmetric homobilayers are part of Table II. In particular, the Rashba parameters are of the order of tens or a few hundred meV/Å, greatly exceeding the moiré bandwidth at small angles. Therefore, in the small-angle regime, Rashba effects are likely to affect, if not dominate, the correlated physics of these systems.

III. DISCUSSION

In conclusion, we have presented an extended continuum model able to accurately calculate the electronic structure of twisted Janus TMDs. The model features terms that properly take into account lattice relaxation, the stacking dependence of the effective mass, and Rashba spin-orbit coupling. The application of this methodology to more than a hundred twisted bilayers reveals the richness of their physics, and that it can be carefully tuned by choosing atomic composition, stacking structure, interface ordering, and twist angle.

In symmetrically ordered homobilayers, the layers' inversion symmetry prevents Rashba spin splittings and allows for the emergence of symmetries and Dirac nodes in the moiré bands. Thus they are able to realize not only common triangular moiré superlattices but also honeycomb and kagome networks [78], potentially displaying rich correlated-electronic phenomena and enabling their use as a platform of quantum simulators [35]. The honeycomb bands that form in most 3R twisted homobilayers provide a convenient realization of artificial graphene, but with a fine-structure constant that can be tuned at will simply by varying twist angle [79]. The kagome lattice models of 3R WSSe and MoSSe are expected to host different phases, including spin liquids [75,76]. Furthermore, by manipulating spin-orbit coupling with gate electric fields or by proximity effects, these bands can exhibit topologically nontrivial states [80–83]. Since all systems have bandwidths that can be adjusted simply by varying twist angles, they provide an enticing toolbox to study the exotic properties of strongly correlated physics in hexagonal Bravais lattices [84–88].

In heterobilayers and asymmetrically ordered homobilayers, Rashba spin-orbit coupling constants can greatly exceed the systems' bandwidth, therefore being expected to have an important impact on the correlated states. Indeed, this situation could provide opportunities for observing nontrivial phenomena such as the intrinsic spin Hall effect [89], noncentrosymmetric superconductivity [90], and Majorana fermions [91]. Furthermore, the presence of a magnetic substrate can strongly impact the noncoplanar magnetic texture of the moiré unit cell [92], providing an additional degree of freedom to tune the system's properties.

Additionally, light-matter interactions can have a significant impact on the bilayer physics [93–96]. This is because the quenching of the kinetic energy of flatband electrons might allow one to reach the regime of strong light-matter interactions more easily than in dispersive materials.

Finally, with the data employed in the continuum model calculations and shown in Tables II and III, we present a step toward the creation of a twistronics database, containing data from different systems and able to calculate properties for any, including arbitrarily small, twist angles. This information can serve as a basis for guiding both theoretical and experimental studies, relevant to different research strategies, such as direct and inverse design, and artificial intelligence investigations [36,97]. We expect our results to have implications for the theoretical and experimental study of correlated physics in moiré materials, which could pave the way for the use of these systems for magnetism, spintronics, and other nanoscale devices.

[1] V. L. Ginzburg, Nobel lecture: On superconductivity and superfluidity (what I have and have not managed to do) as well as on the "physical minimum" at the beginning of the XXI century, Rev. Mod. Phys. **76**, 981 (2004).

[2] H. L. Stormer, Nobel lecture: The fractional quantum Hall effect, Rev. Mod. Phys. **71**, 875 (1999).

[3] B. Keimer and J. E. Moore, The physics of quantum materials, Nat. Phys. **13**, 1045 (2017).

[4] D. N. Basov, R. D. Averitt, and D. Hsieh, Towards properties on demand in quantum materials, Nat. Mater. **16**, 1077 (2017).

[5] F. Giustino, J. H. Lee, F. Trier, M. Bibes, S. M. Winter, R. Valentí, Y.-W. Son, L. Taillefer, C. Heil, A. I. Figueroa, B. Plaçais, Q. Wu, O. V. Yazyev, E. P. A. M. Bakkers, J. Nygård, P. Forn-Díaz, S. D. Franceschi, J. W. McIver, L. E. F. F. Torres, T. Low *et al.*, The 2021 quantum materials roadmap, J. Phys. Mater. **3**, 042006 (2020).

[6] Y. Cao, V. Fatemi, A. Demir, S. Fang, S. L. Tomarken, J. Y. Luo, J. D. Sanchez-Yamagishi, K. Watanabe, T. Taniguchi, E. Kaxiras, R. C. Ashoori, and P. Jarillo-Herrero, Correlated insulator behaviour at half-filling in magic-angle graphene superlattices, Nature (London) **556**, 80 (2018).

[7] Y. Cao, V. Fatemi, S. Fang, K. Watanabe, T. Taniguchi, E. Kaxiras, and P. Jarillo-Herrero, Unconventional superconductivity in magic-angle graphene superlattices, Nature (London) **556**, 43 (2018).

[8] X. Lu, P. Stepanov, W. Yang, M. Xie, M. A. Aamir, I. Das, C. Urgell, K. Watanabe, T. Taniguchi, G. Zhang, A. Bachtold, A. H. MacDonald, and D. K. Efetov, Superconductors, orbital magnets and correlated states in magic-angle bilayer graphene, Nature (London) **574**, 653 (2019).

[9] M. He, Y.-H. Zhang, Y. Li, Z. Fei, K. Watanabe, T. Taniguchi, X. Xu, and M. Yankowitz, Competing correlated states and abundant orbital magnetism in twisted monolayer-bilayer graphene, Nat. Commun. **12**, 4727 (2021).

[10] M. Yankowitz, S. Chen, H. Polshyn, Y. Zhang, K. Watanabe, T. Taniguchi, D. Graf, A. F. Young, and C. R. Dean, Tuning superconductivity in twisted bilayer graphene, Science **363**, 1059 (2019).

[11] H. Zhou, T. Xie, T. Taniguchi, K. Watanabe, and A. F. Young, Superconductivity in rhombohedral trilayer graphene, Nature (London) **598**, 434 (2021).

[12] J. M. Park, Y. Cao, K. Watanabe, T. Taniguchi, and P. Jarillo-Herrero, Tunable strongly coupled superconductivity in magic-angle twisted trilayer graphene, Nature (London) **590**, 249 (2021).

[13] R. Li, Y. Cheng, and W. Huang, Recent progress of Janus 2D transition metal chalcogenides: From theory to experiments, Small **14**, 1802091 (2018).

[14] A. C. Gadelha, D. A. A. Ohlberg, C. Rabelo, E. G. S. Neto, T. L. Vasconcelos, J. L. Campos, J. S. Lemos, V. Ornelas, D. Miranda, R. Nadas, F. C. Santana, K. Watanabe, T. Taniguchi, B. van Troeye, M. Lamparski, V. Meunier, V.-H. Nguyen, D. Paszko, J.-C. Charlier, L. C. Campos *et al.*, Localization of lattice dynamics in low-angle twisted bilayer graphene, Nature (London) **590**, 405 (2021).

[15] Y. Saito, J. Ge, K. Watanabe, T. Taniguchi, and A. F. Young, Independent superconductors and correlated insulators in twisted bilayer graphene, Nat. Phys. **16**, 926 (2020).

[16] D. Wong, K. P. Nuckolls, M. Oh, B. Lian, Y. Xie, S. Jeon, K. Watanabe, T. Taniguchi, B. A. Bernevig, and A. Yazdani, Cascade of electronic transitions in magic-angle twisted bilayer graphene, Nature (London) **582**, 198 (2020).

[17] E. Y. Andrei, D. K. Efetov, P. Jarillo-Herrero, A. H. MacDonald, K. F. Mak, T. Senthil, E. Tutuc, A. Yazdani, and A. F. Young, The marvels of moiré materials, Nat. Rev. Mater. **6**, 201 (2021).

[18] S. Carr, S. Fang, and E. Kaxiras, Electronic-structure methods for twisted moiré layers, Nat. Rev. Mater. **5**, 748 (2020).

[19] C. N. Lau, M. W. Bockrath, K. F. Mak, and F. Zhang, Reproducibility in the fabrication and physics of moiré materials, Nature (London) **602**, 41 (2022).

[20] R. Bistritzer and A. H. MacDonald, Moiré bands in twisted double-layer graphene, Proc. Natl. Acad. Sci. USA **108**, 12233 (2011).

[21] S. Carr, D. Massatt, S. Fang, P. Cazeaux, M. Luskin, and E. Kaxiras, Twistronics: Manipulating the electronic properties of two-dimensional layered structures through their twist angle, Phys. Rev. B **95**, 075420 (2017).

[22] Z. Song, Z. Wang, W. Shi, G. Li, C. Fang, and B. A. Bernevig, All Magic Angles in Twisted Bilayer Graphene are Topological, Phys. Rev. Lett. **123**, 036401 (2019).

[23] M. Angeli, D. Mandelli, A. Valli, A. Amaricci, M. Capone, E. Tosatti, and M. Fabrizio, Emergent D_6 symmetry in fully relaxed magic-angle twisted bilayer graphene, Phys. Rev. B **98**, 235137 (2018).

[24] H. C. Po, L. Zou, A. Vishwanath, and T. Senthil, Origin of Mott Insulating Behavior and Superconductivity in Twisted Bilayer Graphene, Phys. Rev. X **8**, 031089 (2018).

[25] M. Angeli, E. Tosatti, and M. Fabrizio, Valley Jahn-Teller Effect in Twisted Bilayer Graphene, Phys. Rev. X **9**, 041010 (2019).

[26] H. Yoo, R. Engelke, S. Carr, S. Fang, K. Zhang, P. Cazeaux, S. H. Sung, R. Hovden, A. W. Tsen, T. Taniguchi, K. Watanabe, G.-C. Yi, M. Kim, M. Luskin, E. B. Tadmor, E. Kaxiras, and P. Kim, Atomic and electronic reconstruction at the van der Waals interface in twisted bilayer graphene, Nat. Mater. **18**, 448 (2019).

[27] B. Lian, Z. Wang, and B. A. Bernevig, Twisted Bilayer Graphene: A Phonon-Driven Superconductor, Phys. Rev. Lett. **122**, 257002 (2019).

[28] A. Blason and M. Fabrizio, Local Kekulé distortion turns twisted bilayer graphene into topological Mott insulators and superconductors, Phys. Rev. B **106**, 235112 (2022).

[29] A. Ghiotto, E.-M. Shih, G. S. S. G. Pereira, D. A. Rhodes, B. Kim, J. Zang, A. J. Millis, K. Watanabe, T. Taniguchi, J. C. Hone, L. Wang, C. R. Dean, and A. N. Pasupathy, Quantum criticality in twisted transition metal dichalcogenides, Nature (London) **597**, 345 (2021).

[30] M. Grzeszczyk, J. Szpakowski, A. O. Slobodeniuk, T. Kazimierczuk, M. Bhatnagar, T. Taniguchi, K. Watanabe, P. Kossacki, M. Potemski, A. Babiński, and M. R. Molas, The optical response of artificially twisted MoS$_2$ bilayers, Sci. Rep. **11**, 17037 (2021).

[31] Y. Xu, K. Kang, K. Watanabe, T. Taniguchi, K. F. Mak, and J. Shan, Tunable bilayer Hubbard model physics in twisted WSe2, Nat. Nanotechnol. **17**, 934 (2022).

[32] Y. Tang, L. Li, T. Li, Y. Xu, S. Liu, K. Barmak, K. Watanabe, T. Taniguchi, A. H. MacDonald, J. Shan, and K. F. Mak, Simulation of Hubbard model physics in WSe$_2$/WS$_2$ moiré superlattices, Nature (London) **579**, 353 (2020).

[33] L. Wang, E.-M. Shih, A. Ghiotto, L. Xian, D. A. Rhodes, C. Tan, M. Claassen, D. M. Kennes, Y. Bai, B. Kim, K. Watanabe, T. Taniguchi, X. Zhu, J. Hone, A. Rubio, A. N. Pasupathy, and C. R. Dean, Correlated electronic phases in twisted bilayer transition metal dichalcogenides, Nat. Mater. **19**, 861 (2020).

[34] K. Tran, G. Moody, F. Wu, X. Lu, J. Choi, K. Kim, A. Rai, D. A. Sanchez, J. Quan, A. Singh, J. Embley, A. Zepeda, M. Campbell, T. Autry, T. Taniguchi, K. Watanabe, N. Lu, S. K. Banerjee, K. L. Silverman, S. Kim *et al.*, Evidence for moiré excitons in van der Waals heterostructures, Nature (London) **567**, 71 (2019).

[35] D. M. Kennes, M. Claassen, L. Xian, A. Georges, A. J. Millis, J. Hone, C. R. Dean, D. N. Basov, A. N. Pasupathy, and A. Rubio, Moiré heterostructures as a condensed-matter quantum simulator, Nat. Phys. **17**, 155 (2021).

[36] G. A. Tritsaris, S. Carr, and G. R. Schleder, Computational design of moiré assemblies aided by artificial intelligence, Appl. Phys. Rev. **8**, 031401 (2021).

[37] R. K. Defo, S. Fang, S. N. Shirodkar, G. A. Tritsaris, A. Dimoulas, and E. Kaxiras, Strain dependence of band gaps and exciton energies in pure and mixed transition-metal dichalcogenides, Phys. Rev. B **94**, 155310 (2016).

[38] J. Zhang, S. Jia, I. Kholmanov, L. Dong, D. Er, W. Chen, H. Guo, Z. Jin, V. B. Shenoy, L. Shi, and J. Lou, Janus monolayer transition-metal dichalcogenides, ACS Nano **11**, 8192 (2017).

[39] F. Wu, T. Lovorn, E. Tutuc, and A. H. MacDonald, Hubbard Model Physics in Transition Metal Dichalcogenide Moiré Bands, Phys. Rev. Lett. **121**, 026402 (2018).

[40] M. Angeli and A. H. MacDonald, γ-valley transition metal dichalcogenide moiré bands, Proc. Natl. Acad. Sci. **118**, e2021826118 (2021).

[41] N. C. Hu and A. H. MacDonald, Competing magnetic states in transition metal dichalcogenide moiré materials, Phys. Rev. B **104**, 214403 (2021).

[42] J. Zang, J. Wang, J. Cano, and A. J. Millis, Hartree-Fock study of the moiré Hubbard model for twisted bilayer transition metal dichalcogenides, Phys. Rev. B **104**, 075150 (2021).

[43] H. Pan, F. Wu, and S. Das Sarma, Band topology, Hubbard model, Heisenberg model, and Dzyaloshinskii-Moriya interaction in twisted bilayer WSe$_2$, Phys. Rev. Res. **2**, 033087 (2020).

[44] S. Liu, E. Khalaf, J. Y. Lee, and A. Vishwanath, Nematic topological semimetal and insulator in magic-angle bilayer graphene at charge neutrality, Phys. Rev. Res. **3**, 013033 (2021).

[45] N. Bultinck, E. Khalaf, S. Liu, S. Chatterjee, A. Vishwanath, and M. P. Zaletel, Ground State and Hidden Symmetry of Magic-Angle Graphene at Even Integer Filling, Phys. Rev. X **10**, 031034 (2020).

[46] F. Xie, N. Regnault, D. Călugăru, B. A. Bernevig, and B. Lian, Twisted symmetric trilayer graphene. II. Projected Hartree-Fock study, Phys. Rev. B **104**, 115167 (2021).

[47] Y. Zhang, K. Jiang, Z. Wang, and F. Zhang, Correlated insulating phases of twisted bilayer graphene at commensurate filling fractions: A Hartree-Fock study, Phys. Rev. B **102**, 035136 (2020).

[48] N. Morales-Durán, A. H. MacDonald, and P. Potasz, Metal-insulator transition in transition metal dichalcogenide heterobilayer moiré superlattices, Phys. Rev. B **103**, L241110 (2021).

[49] N. Morales-Durán, N. C. Hu, P. Potasz, and A. H. MacDonald, Nonlocal Interactions in Moiré Hubbard Systems, Phys. Rev. Lett. **128**, 217202 (2022).

[50] S. Carr, S. Fang, H. C. Po, A. Vishwanath, and E. Kaxiras, Derivation of Wannier orbitals and minimal-basis tight-binding Hamiltonians for twisted bilayer graphene: First-principles approach, Phys. Rev. Res. **1**, 033072 (2019).

[51] D. M. Kennes, J. Lischner, and C. Karrasch, Strong correlations and $d + id$ superconductivity in twisted bilayer graphene, Phys. Rev. B **98**, 241407(R) (2018).

[52] L. Xian, M. Claassen, D. Kiese, M. M. Scherer, S. Trebst, D. M. Kennes, and A. Rubio, Realization of nearly dispersionless bands with strong orbital anisotropy from destructive interference in twisted bilayer MoS_2, Nat. Commun. **12**, 5644 (2021).

[53] D. M. Kennes, L. Xian, M. Claassen, and A. Rubio, One-dimensional flat bands in twisted bilayer germanium selenide, Nat. Commun. **11**, 1124 (2020).

[54] M. Claassen, L. Xian, D. M. Kennes, and A. Rubio, Ultra-strong spin–orbit coupling and topological moiré engineering in twisted ZrS_2 bilayers, Nat. Commun. **13**, 4915 (2022).

[55] L. Xian, D. M. Kennes, N. Tancogne-Dejean, M. Altarelli, and A. Rubio, Multiflat bands and strong correlations in twisted bilayer boron nitride: Doping-induced correlated insulator and superconductor, Nano Lett. **19**, 4934 (2019).

[56] T. Soejima, D. E. Parker, N. Bultinck, J. Hauschild, and M. P. Zaletel, Efficient simulation of moiré materials using the density matrix renormalization group, Phys. Rev. B **102**, 205111 (2020).

[57] A. Weston, Y. Zou, V. Enaldiev, A. Summerfield, N. Clark, V. Zólyomi, A. Graham, C. Yelgel, S. Magorrian, M. Zhou, J. Zultak, D. Hopkinson, A. Barinov, T. H. Bointon, A. Kretinin, N. R. Wilson, P. H. Beton, V. I. Fal'ko, S. J. Haigh, and R. Gorbachev, Atomic reconstruction in twisted bilayers of transition metal dichalcogenides, Nat. Nanotechnol. **15**, 592 (2020).

[58] A. S. Nowick, *Crystal Properties via Group Theory* (Cambridge University Press, Cambridge, England, 1995).

[59] W. Zhou, J. Chen, Z. Yang, J. Liu, and F. Ouyang, Geometry and electronic structure of monolayer, bilayer, and multilayer Janus WSSe, Phys. Rev. B **99**, 075160 (2019).

[60] J. Jung, A. Raoux, Z. Qiao, and A. H. MacDonald, Ab initio theory of moiré superlattice bands in layered two-dimensional materials, Phys. Rev. B **89**, 205414 (2014).

[61] S. Carr, D. Massatt, S. B. Torrisi, P. Cazeaux, M. Luskin, and E. Kaxiras, Relaxation and domain formation in incommensurate two-dimensional heterostructures, Phys. Rev. B **98**, 224102 (2018).

[62] A. Kormányos, G. Burkard, M. Gmitra, J. Fabian, V. Zólyomi, N. D. Drummond, and V. Fal'ko, $k \cdot p$ theory for two-dimensional transition metal dichalcogenide semiconductors, 2D Mater. **2**, 022001 (2015).

[63] P. Giannozzi, S. Baroni, N. Bonini, M. Calandra, R. Car, C. Cavazzoni, D. Ceresoli, G. L. Chiarotti, M. Cococcioni, I. Dabo, A. D. Corso, S. de Gironcoli, S. Fabris, G. Fratesi, R. Gebauer, U. Gerstmann, C. Gougoussis, A. Kokalj, M. Lazzeri, L. Martin-Samos *et al.*, QUANTUM ESPRESSO: A modular and open-source software project for quantum simulations of materials, J. Phys.: Condens. Matter **21**, 395502 (2009).

[64] P. Giannozzi, O. Andreussi, T. Brumme, O. Bunau, M. B. Nardelli, M. Calandra, R. Car, C. Cavazzoni, D. Ceresoli, M. Cococcioni, N. Colonna, I. Carnimeo, A. D. Corso, S. de Gironcoli, P. Delugas, R. A. DiStasio, A. Ferretti, A. Floris, G. Fratesi, G. Fugallo *et al.*, Advanced capabilities for materials modelling with quantum ESPRESSO, J. Phys.: Condens. Matter **29**, 465901 (2017).

[65] I. Hamada and M. Otani, Comparative van der Waals density-functional study of graphene on metal surfaces, Phys. Rev. B **82**, 153412 (2010).

[66] K. Berland, V. R. Cooper, K. Lee, E. Schröder, T. Thonhauser, P. Hyldgaard, and B. I. Lundqvist, van der Waals forces in density functional theory: A review of the vdW-DF method, Rep. Prog. Phys. **78**, 066501 (2015).

[67] See Supplemental Material at http://link.aps.org/supplemental/10.1103/PhysRevB.106.235159 for comparison between continuum model and DFT band structures, for details on the effect of relaxation on the generalized stacking fault energy (GSFE), for band structures of selected twisted 2H homobilayers with symmetric ordering, and for band structures of selected asymmetrically ordered twisted bilayers showing their spin polarization.

[68] S. Zhou, J. Han, S. Dai, J. Sun, and D. J. Srolovitz, van der Waals bilayer energetics: Generalized stacking-fault energy of graphene, boron nitride, and graphene/boron nitride bilayers, Phys. Rev. B **92**, 155438 (2015).

[69] E. Kaxiras and M. S. Duesbery, Free Energies of Generalized Stacking Faults in Si and Implications for the Brittle-Ductile Transition, Phys. Rev. Lett. **70**, 3752 (1993).

[70] H. Tang, S. Carr, and E. Kaxiras, Geometric origins of topological insulation in twisted layered semiconductors, Phys. Rev. B **104**, 155415 (2021).

[71] L. Zou, H. C. Po, A. Vishwanath, and T. Senthil, Band structure of twisted bilayer graphene: Emergent symmetries, commensurate approximants, and Wannier obstructions, Phys. Rev. B **98**, 085435 (2018).

[72] M. Angeli and M. Fabrizio, Jahn-Teller coupling to moiré phonons in the continuum model formalism for small-angle twisted bilayer graphene, Eur. Phys. J. Plus **135**, 630 (2020).

[73] B. Bradlyn, L. Elcoro, J. Cano, M. G. Vergniory, Z. Wang, C. Felser, M. I. Aroyo, and B. A. Bernevig, Topological quantum chemistry, Nature (London) **547**, 298 (2017).

[74] L. Elcoro, B. Bradlyn, Z. Wang, M. G. Vergniory, J. Cano, C. Felser, B. A. Bernevig, D. Orobengoa, G. de la Flor, and M. I. Aroyo, Double crystallographic groups and their representations on the Bilbao crystallographic server, J. Appl. Cryst. **50**, 1457 (2017).

[75] T.-H. Han, J. S. Helton, S. Chu, D. G. Nocera, J. A. Rodriguez-Rivera, C. Broholm, and Y. S. Lee, Fractionalized excitations in the spin-liquid state of a kagome-lattice antiferromagnet, Nature (London) **492**, 406 (2012).

[76] C. Broholm, R. J. Cava, S. A. Kivelson, D. G. Nocera, M. R. Norman, and T. Senthil, Quantum spin liquids, Science **367**, eaay0668 (2020).

[77] A. H. Castro Neto, F. Guinea, N. M. R. Peres, K. S. Novoselov, and A. K. Geim, The electronic properties of graphene, Rev. Mod. Phys. **81**, 109 (2009).

[78] F. Crasto de Lima, R. H. Miwa, and E. Suárez Morell, Double flat bands in kagome twisted bilayers, Phys. Rev. B **100**, 155421 (2019).

[79] G. W. Semenoff, Chiral symmetry breaking in graphene, Phys. Scr. **2012**, 014016 (2012).

[80] E. Tang, J.-W. Mei, and X.-G. Wen, High-Temperature Fractional Quantum Hall States, Phys. Rev. Lett. **106**, 236802 (2011).

[81] S. Iimura and Y. Imai, Thermal Hall conductivity in superconducting phase on kagome lattice, J. Phys. Soc. Jpn. **87**, 094715 (2018).

[82] C. L. Kane and E. J. Mele, Quantum Spin Hall Effect in Graphene, Phys. Rev. Lett. **95**, 226801 (2005).

[83] Z. F. Wang, Z. Liu, and F. Liu, Quantum Anomalous Hall Effect in 2D Organic Topological Insulators, Phys. Rev. Lett. **110**, 196801 (2013).

[84] C. Wu, Orbital Ordering and Frustration of p-Band Mott Insulators, Phys. Rev. Lett. **100**, 200406 (2008).

[85] G.-F. Zhang, Y. Li, and C. Wu, Honeycomb lattice with multiorbital structure: Topological and quantum anomalous Hall insulators with large gaps, Phys. Rev. B **90**, 075114 (2014).

[86] J. Wen, A. Rüegg, C.-C. Joseph Wang, and G. A. Fiete, Interaction-driven topological insulators on the kagome and the decorated honeycomb lattices, Phys. Rev. B **82**, 075125 (2010).

[87] W. M. H. Natori, R. Nutakki, R. G. Pereira, and E. C. Andrade, SU(4) Heisenberg model on the honeycomb lattice with exchange-frustrated perturbations: Implications for twistronics and Mott insulators, Phys. Rev. B **100**, 205131 (2019).

[88] M. L. Kiesel, C. Platt, and R. Thomale, Unconventional Fermi Surface Instabilities in the Kagome Hubbard Model, Phys. Rev. Lett. **110**, 126405 (2013).

[89] J. Sinova, D. Culcer, Q. Niu, N. A. Sinitsyn, T. Jungwirth, and A. H. MacDonald, Universal Intrinsic Spin Hall Effect, Phys. Rev. Lett. **92**, 126603 (2004).

[90] E. Bauer, G. Hilscher, H. Michor, C. Paul, E. W. Scheidt, A. Gribanov, Y. Seropegin, H. Noël, M. Sigrist, and P. Rogl, Heavy Fermion Superconductivity and Magnetic Order in Noncentrosymmetric $CePt_3Si$, Phys. Rev. Lett. **92**, 027003 (2004).

[91] M. Sato and S. Fujimoto, Topological phases of noncentrosymmetric superconductors: Edge states, Majorana fermions, and non-Abelian statistics, Phys. Rev. B **79**, 094504 (2009).

[92] D. Soriano and J. L. Lado, Spin–orbit correlations and exchange-bias control in twisted Janus dichalcogenide multilayers, New J. Phys. **23**, 073038 (2021).

[93] G. E. Topp, C. J. Eckhardt, D. M. Kennes, M. A. Sentef, and P. Törmä, Light-matter coupling and quantum geometry in moiré materials, Phys. Rev. B **104**, 064306 (2021).

[94] G. E. Topp, G. Jotzu, J. W. McIver, L. Xian, A. Rubio, and M. A. Sentef, Topological Floquet engineering of twisted bilayer graphene, Phys. Rev. Res. **1**, 023031 (2019).

[95] S. Latini, E. Ronca, U. De Giovannini, H. Hübener, and A. Rubio, Cavity control of excitons in two-dimensional materials, Nano Lett. **19**, 3473 (2019).

[96] Y. Li, H. A. Fertig, and B. Seradjeh, Floquet-engineered topological flat bands in irradiated twisted bilayer graphene, Phys. Rev. Res. **2**, 043275 (2020).

[97] G. R. Schleder, B. Focassio, and A. Fazzio, Machine learning for materials discovery: Two-dimensional topological insulators, Appl. Phys. Rev. **8**, 031409 (2021).